

# Method for controlled tissue theranostics using a single tunable laser source

**ROK PODLIPEC,<sup>1,2</sup> JAKA MUR,<sup>3</sup>  JAKA PETELIN,<sup>3</sup> JANEZ ŠTRANCAR,<sup>1</sup> AND ROK PETKOVŠEK<sup>3,\*</sup> **

<sup>1</sup>Laboratory of Biophysics, Condensed Matter Physics Department, Jožef Stefan Institute, Jamova cesta 39, Ljubljana, Slovenia

<sup>2</sup>Helmholtz-Zentrum Dresden-Rossendorf e.V., Ion Beam Center, Bautzner Landstraße 400, Dresden 01328, Germany

<sup>3</sup>Faculty of Mechanical Engineering, University of Ljubljana, Aškerčeva 6, Ljubljana, Slovenia

\*[rok.petkovsek@fs.uni-lj.si](mailto:rok.petkovsek@fs.uni-lj.si)

**Abstract:** Tissue diseases and related disorders need to be first recognized using diagnostic methods and then later treated by therapeutic methods—a joint procedure called theranostics. One of the main challenges in the field of retinal therapies remains in the success of the treatment, typically improving the local metabolism, by sparing the surrounding tissue and with the immediate information of the laser effect. In our study, we present a concept for real-time controlled tissue theranostics on a proof-of-concept study capable of using a single tunable ps laser source (in terms of irradiance, fluence, and repetition rate), done on ex-vivo human retinal pigment epithelium. We have found autofluorescence intensity and lifetime imaging diagnostics very promising for the recognition and quantification of laser effects ranging from selective non-destructive molecular tissue modification to complete tissue ablation. The main novelty of our work presents the developed algorithm for optimized theranostics based on the model function used to quantify laser-induced tissue changes through the diagnostics descriptors, fluorescence lifetime and fluorescence intensity parameters. This approach, together with the operation of the single adaptable laser source, can serve as a new theranostics method in personalized medicine in the future not only limited to treat retinal diseases.

© 2021 Optical Society of America under the terms of the [OSA Open Access Publishing Agreement](#)

## 1. Introduction

Recent advances in sensitive, less intrusive diagnostic methods using efficient and highly resolved imaging, reliable algorithms for image processing and recognition of pathologies [1], as well as controlled, repeatable therapeutic effects made progress in various fields of medicine. The goal of the described combination of diagnostics and therapy, in short theranostics, is in individualization and selectivity of the processes, leading to better treatment results [2].

Non-destructive application of non-ionizing radiation using low photon energy, low peak irradiance, and the low dose is a promising tool for the diagnosis of pathologies on a sub-cellular scale, even in ultrasensitive sensorial tissue, tissues located away from the body surface, or both, such as the retina. Microwave radiation does not provide a high enough resolution, far IR light is strongly absorbed in the water-based tissues, leaving NIR and visible light as the most suitable choices [3,4]. Diagnostic methods evolved around two approaches, the first based on tissue autofluorescence in the visual part of the spectrum [5] and the second based on interferometric imaging with NIR light [6]. In the second class, OCT (Optical Coherence Tomography) is widely used and it has been developed to be an advanced imaging tool, even for 3D imaging [7]. The physical principle of OCT, based on scattered light interference, prevents identification of certain pathologies and associated supramolecular structures [8].

On the other hand, methods based on molecular fluorescence have the potential to provide not only morphological information but pathology-associated information as well. For example, fundus autofluorescence (FAF) and especially modern advanced time-resolved fluorescence lifetime imaging ophthalmoscopy (FLIO), realized as Spectralis by Heidelberg Engineering [9–11]), can provide information beyond other common multimodal imaging/diagnostics techniques [12,13].

Fluorescence lifetime imaging microscopy (FLIM) evolved around intensity-modulated CW lasers and synchronous phase-sensitive detection [14], while novel techniques rely on ultrashort pulsed laser sources [15], working at high repetition rates from few MHz [16] to around 100 MHz [17], encompassing typical repetition rates of mode-locked oscillators. The lifetimes are determined through the acquisition of a time-histogram of emitted photon delays by the time-correlated single photon counting (TCSPC) module [18]. In this case, the high repetition rate is essential to ensure timely detection of the rare photons of endogenous biological fluorescence [12,19], while keeping fluence low, not to disrupt sample by photochemical, photothermal or photomechanical effects and to still acquire a sufficient S/N ratio [20]. To improve light transmission and localization of the excitation site, typically the mode-locked femtosecond two-photon laser sources can be used instead of one-photon. They provide sufficient energy per pulse on the order of tens of nJ at an acceptably high repetition rate [17,21] but are costly due to their complexity. Contrary to these requirements, high pulse energies are needed to introduce enough energy into the tissue to create localized therapeutic effects ranging from photothermal to photomechanical inducing rapid vaporization [22]. Commonly used laser sources have a pulse duration longer than ns, typically of  $\mu$ s (for selective retinal therapy [23]) or even ms length (for pan retinal photocoagulation [24]), both applied with a low repetition rate of typically less than 100 Hz to allow thermal relaxation. However, short ps lasers have as well been tested for an intraocular tissue therapy via photodisruption with considerably reduced side effects compared to longer ns lasers [25], making them promising for applications of this kind.

Such diametrical properties of laser systems used in retinal diagnostics and therapy, first lacking in flexibility and second in repetition rate, can easily rule out the possibility of having a single laser system for both diagnostics and therapy. By such a laser system, faster theranostics would be feasible, with less impact of the movement of the targeted tissue, keeping the focus for both diagnostics and therapy the same with minimal damage introduced to the surrounding tissue. Furthermore, the same laser would keep the treatment spot exactly on the diagnosed pathological state. With typically different lasers used consecutively, this is commonly not the case and adaptive optics (AO) needs to be used to align and focus both lasers on the same spot due to aberrations, etc. However, a few standard methods to access the tissue effect of the treatment laser in automatic feedback control have been developed which are based on optoacoustic detection of the formation of microbubbles [26] and optical coherence tomography detection of bubble-related tissue displacement [27].

The goal of our work was to develop a concept for real-time controlled tissue theranostics using a single tunable and cost effective laser source – joining diagnostic autofluorescence (AF) microscopy with laser-based treatment. We report on low-power high repetition rate AF imaging combined with precise high-power adjustable repetition rate photo-induced treatment, using a custom picosecond compact MOPA fiber laser based on a gain switch DFB laser diode (MOPA GS fiber laser). We installed the laser into a nonlinear microscopy setup, allowing potential two-photon excitation and FLIM detection. FLIM has been previously proven to work by a two-photon excitation, with the fluorescence lifetime remaining the same as excited with one-photon excitation [28,29]. The aim was to use FLIM for the characterization of laser-induced tissue effects, not capable with the intensity-based autofluorescence imaging. Using the treatment mode of operation of the laser source with wide laser parameter space, the aim was also to achieve selective tissue/cell modification.

## 2. Experimental setup

### 2.1. Theranostic setup

The theranostic setup was based on a multimodal laser-scanning system (Abberior Instruments; Becker&Hickl), presented in detail in our previous work [30], and schematically represented in Fig. 1. The imaging part of the system employed two fluorescence excitation units: a low power single-photon excitation laser, working at a 561 nm wavelength, emitting 100 ps long pulses at a repetition rate of 80 MHz and maximal average power of 200  $\mu$ W, and a high power two-photon excitation laser (MOPA GS fiber laser), working at a 1030 nm wavelength, emitting 70 ps long pulses at a tuneable repetition rate 100 kHz - 40 MHz and maximal average power of 15W.

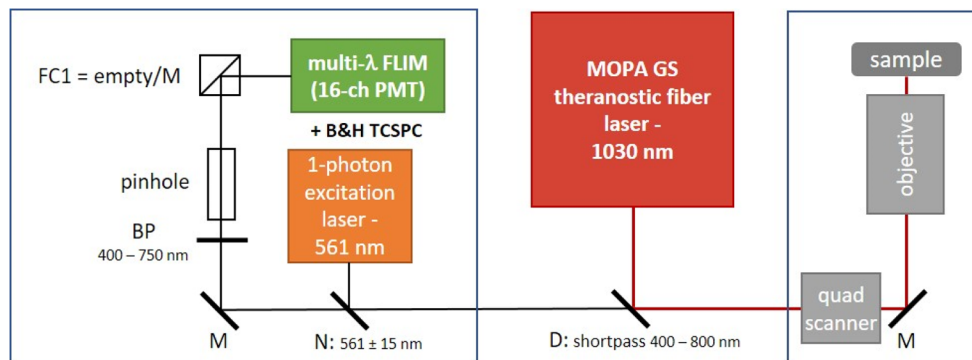


**Fig. 1.** Optical setup schematics. Detection modules are shown in green color. Excitation lasers in orange and red, microscope components in gray. D – dichroic; FC – filter cube; M – mirror; BP – bandpass filter; N – notch filter.

The fluorescence properties were measured using a 16-channel photomultiplier tube (PMT; PML-16-GaAsP, Hamamatsu), coupled with a time-correlated single photon counter unit (TCSPC-SPC-150, Becker&Hickl) for the FLIM and hyperspectral analysis. Since no spectral information was required, signals from all channels were combined for FLIM analysis. The number of time channels were set to 167 with 120 ps time interval, optimally matched to the GaAsP instrument response function (IRF) of 200 ps. Additional bandpass filter was mounted to prevent scattered or reflected light entering the detector system.

Theranostic experiments combining imaging and therapeutic modalities were performed on the same time or consecutively through the same 10x magnification objective (Olympus, UPLFLN10, 10 mm working distance, numerical aperture 0.3) in a laser scanning mode (Quad Scanner, Abberior Instruments). Fast galvo scanning with pixel dwell time of up to 10  $\mu$ s was used, and more accumulations were added over predefined scan regions in case of a low fluorescence signal (imaging part) or a too weak treatment effect.

The synchronization of the laser excitation pulses with detected photons for the FLIM imaging was done with TCSPC unit [31] connected to Patch Panel (Abberior Instruments) controlled by Inspector software by which we then processed the data through capturing complete fluorescence decay curves in every image pixel. A sufficient detected count number (up to 1000 counts per time channel) and corresponding acceptable S/N ratio were achieved using pixel binning. A compromise between higher binning and the spatial resolution was selected to obtain a desired temporal resolution of the fluorescence lifetimes. Binning of a  $512 \times 512$  pixel images was set to 4, which means  $9 \times 9$  pixels were binned together. The curve fitting using bi-exponential fit was done with software package SPCImage 7.3 (Becker&Hickl), presenting the fitted parameters with colour-coded maps and accompanying histograms. The resulting data is focused on recognizing

the changes in lifetimes and corresponding amplitudes caused by the MOPA GS laser in a controlled targeted treatment.

## 2.2. Laser source

The custom designed MOPA GS fiber laser is a compact all-fiber master-oscillator power-amplifier (MOPA) laser source, based on a gain-switched distributed-feedback (DFB) seed laser diode. The diode is used to generate laser pulses 70 ps long at a repetition rate of up to 40 MHz, using an improved laser design from our previous work (additional details about the laser system design can be found in Ref. [32]). A high-speed electronic circuit was used for precise synchronization and control of both the seed driver and acousto-optic modulator (AOM), as well as the laser pump system control. The laser repetition rate can therefore be set in broad range from 100 kHz to 40 MHz, while the output pulse energy can be set from few nJ up to 20  $\mu$ J, independently of the repetition rate. The relatively high laser pulse energy at all repetition rates requires a continuous control of the optical signal to noise ratio throughout the laser amplifiers chain. The concept allows the laser to emit energy compensated high repetition rate bursts of pulses by compensation of the saturation effect appearing along the amplifier chain. The achieved laser source adaptability and a high output beam quality make the use of a single laser possible for proof of principle theranostics experiments, combining orders of magnitude different operation parameters capable tissue treatment as well as 2-photon diagnostics (see Fig. S1 in the [Supplement 1](#)). The beam quality is independent of the repetition rate and pulse energy used in the scope of the presented experiments and is measured as the beam quality factor  $M^2 = 1.12 \pm 0.06$  according to the ISO 11146-1:2005(E) standard, quantifying the laser beam deviation from an ideal Gaussian beam.

## 2.3. Laser treatment approach

The advantage of fast laser tunability with a broad range of laser parameters was successfully exploited for testing its effects during localized treatment of the targeted retinal tissue. In the first experiment, laser parameters were tuned to the point where we detected the first indication of the treatment effect (Fig. 2), while in the second experiment the effects were observed using a broad range of laser settings (Fig. 3). Laser parameters were swept from low peak irradiance and fluence of  $j = 0.05 \cdot 10^{10}$  W/cm<sup>2</sup> and  $\varepsilon = 0.03$  J/cm<sup>2</sup>, respectively, towards high peak irradiance and fluence of  $j = 5 \cdot 10^{10}$  W/cm<sup>2</sup> and  $\varepsilon = 2$  J/cm<sup>2</sup>, respectively, delivering total energy/dose from  $E = 1$   $\mu$ J to  $E = 1000$   $\mu$ J per pixel. Laser treatment was stopped depending on its effect on the targeted tissue diagnosed with FLIM. Size of the treatment region varied between  $S = 0.01$  mm<sup>2</sup> and  $S = 0.1$  mm<sup>2</sup> inside the image field of view  $S = 0.5$  mm<sup>2</sup>, with the fixed laser scanning step of 1.4  $\mu$ m.

## 2.4. FLIM analysis

Fluorescence lifetime  $\tau_m$  defined as  $\tau_m = a_1\tau_1 + a_2\tau_2$  was obtained from two-component exponential fitting of the experimental curve (Fig. 2(C)), the approach successfully implemented in recent in vivo and ex vivo retinal and RPE autofluorescence studies [20,30] with one difference, lifetime values  $\tau$  being fixed to improve the analysis robustness. Fixed values were chosen from the distribution of initially fitted  $\tau$  across the field of view, taking its mean value (see Fig. S1 B in the [Supplement 1](#)). Mean values of  $\tau_1$  and  $\tau_2$  were almost the same in all measurement sites varying only up to 50-100 ps, which is within the resolution. Fixation of lifetime values didn't drastically affect the goodness of fit shown through least-square distribution  $\chi^2$ , where it remained around 1 in the treatment as well as untreated region (see Fig. S2 A and C in the [Supplement 1](#)).

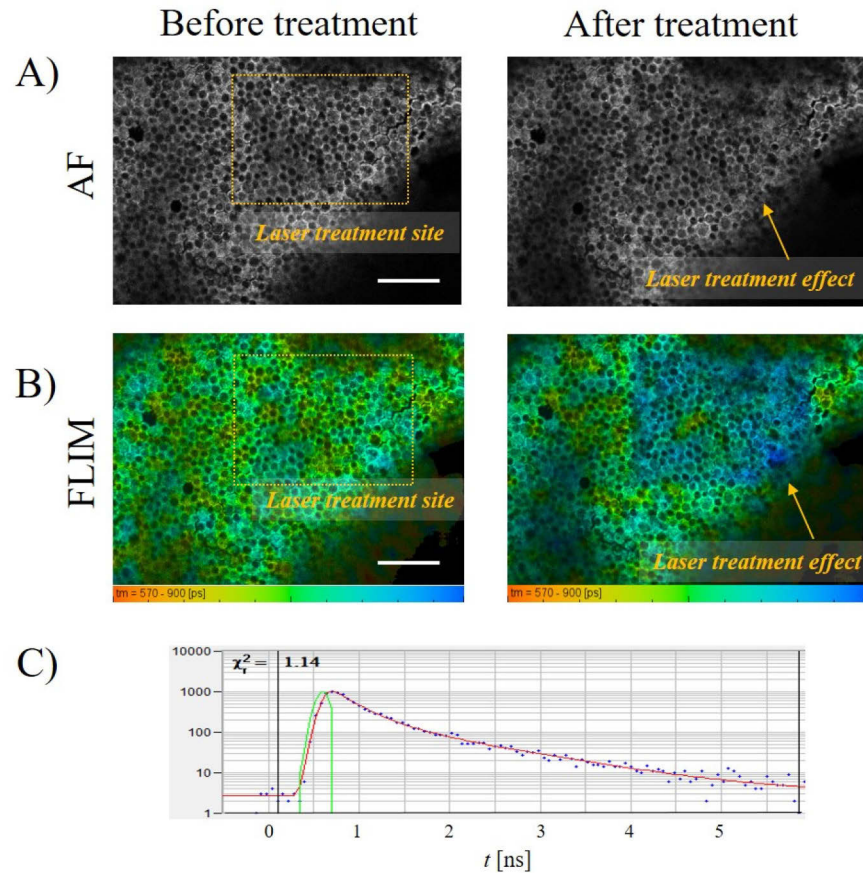


**Fig. 2.** Overperformance of diagnostics capability of fluorescence lifetime imaging microscopy (FLIM) (B) to the conventional autofluorescence imaging (AF) (A) before and after the treatment of ex-vivo human RPE tissue using adaptable MOPA laser system. Predefined treatment site is shown with the yellow rectangle which nicely fits with laser effect observed through the autofluorescence intensity decrease and particularly fluorescence lifetime increase. C) The representative lifetime decay with the corresponding bi-exponential fit. Laser parameters for diagnostics:  $\lambda = 561$  nm,  $t = 100$  ps,  $P = 30$   $\mu$ W,  $\nu = 80$  MHz. Laser parameters for treatment:  $\lambda = 1030$  nm,  $t = 70$  ps,  $P = 100$  mW,  $\nu = 500$  kHz. Scale bar is 100  $\mu$ m.



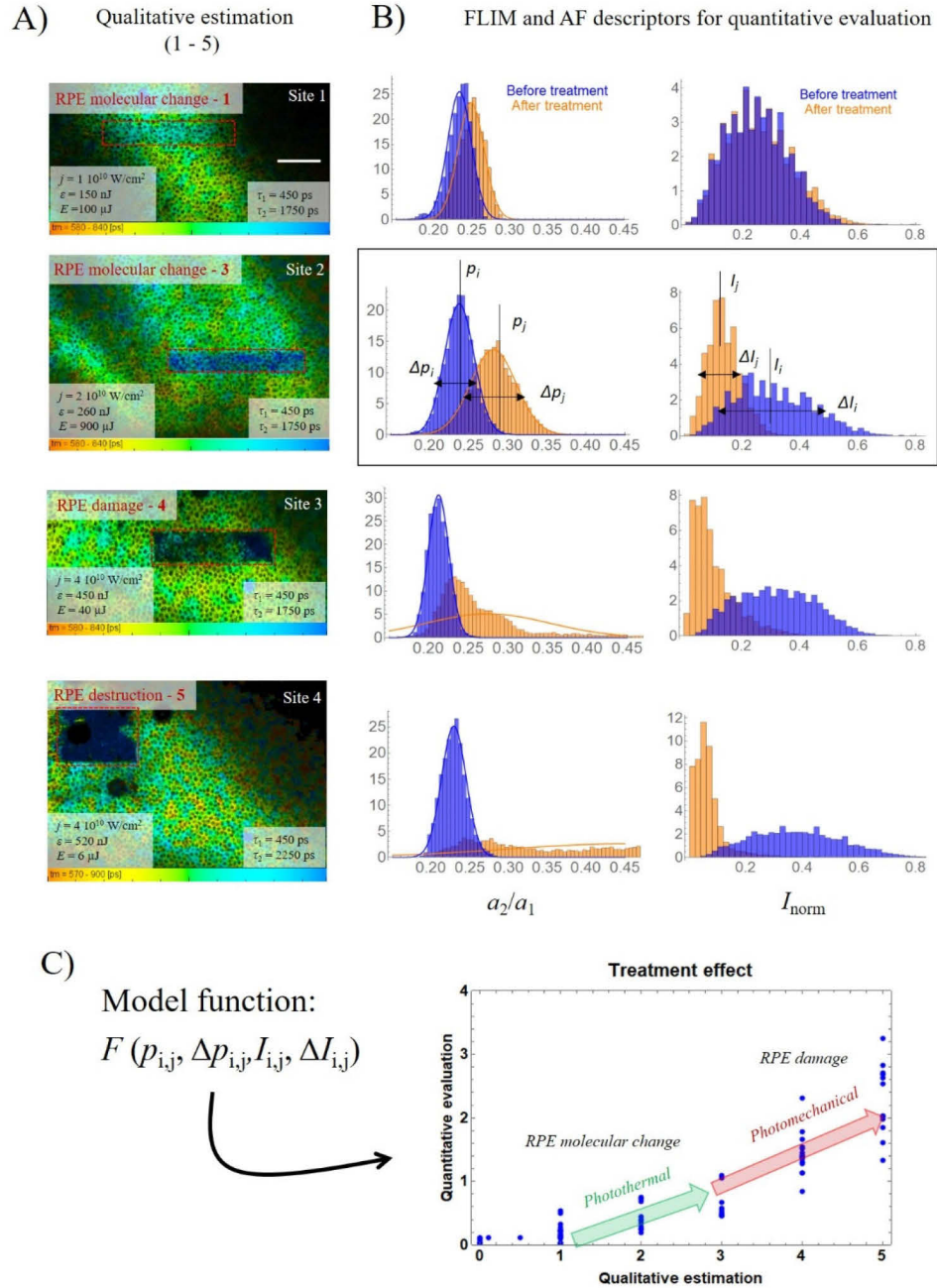


**Fig. 3.** A) Qualitative estimation of the treatment effect of MOPA laser on different sites using different laser settings through the visual assessment of  $\tau_m$  change, with fixated lifetime values  $\tau_1$  and  $\tau_2$ ; B) Distribution histograms of FLIM and AF descriptors that correspond the best to the extent of the laser treatment effect on the tissue through different physical mechanisms; C) Matching of quantitative evaluation of the treatment based on FLIM and AF descriptors with its qualitative estimation. Laser parameters for diagnostics:  $\lambda = 561$  nm,  $t = 100$  ps,  $P = 30$   $\mu$ W,  $\nu = 80$  MHz. The scale bar is 100  $\mu$ m.

### 2.5. Model function for quantification of the treatment effect using diagnostics descriptors

To generalize/implement the described diagnostics approach using AF and FLIM into the frame of automated theranostic procedures, a model function, based on the set of diagnostics descriptors from AF and FLIM data was developed to provide an accurate evaluation and quantification of the treatment effect at any time. Such a combination of model function and tunable laser system that can be adapted in real-time can optimize the treatment and help to avoid unwanted tissue changes. The model function was formulated to correspond best with the linearized qualitative estimation of the treatment effect presented in Fig. 3(A). Both AF and FLIM data were paramount for the model which we present in detail in Section 3.2.

### 2.6. Sample preparation and handling

The proof of principle theranostics studies was performed on ex vivo human retinal tissue. In compliance with the national legislation and with written approval from the patients, we have obtained the samples from the enucleated eyes of the patients with malignant melanoma, requiring whole eye removal. Surgical scissors and razor blade were used to cut the sclera on the eye equator, splitting the eye into two parts by shallow snipping motion all the way around the ball. Considered healthy posterior part of an eye including macula and optical nerve, but excluding vitreous body was fixated by placing it into formalin for 2 hours at room temperature. Fixation was done to preserve the shape, structure and biochemical integrity of the tissue for our complex analysis which needed longer times of measurements and thus non-changing properties of the tissue. After the fixation process, the samples were preserved until the measurements in PBS buffer at 4 °C. Measurements were performed on up to 40 different retinal pigment epithelium (RPE) sites around the macular region not affected by the eye disease on two different enucleated eyes of the patients of the age of 49 and 77. Samples were flipped vertically into humidified 35 mm  $\mu$ -dish (Ibidi) to remain wet state during experiments. The microscope stage temperature was set to 37°C to mimic live retina conditions as much as possible.

## 3. Results and discussion

### 3.1. Measurement of the laser treatment effect using AF and FLIM

To quantify and test the capability of custom-designed MOPA GS fiber laser for the localized tissue treatment, autofluorescence imaging (AF) was performed on ex-vivo human retinal tissue (Fig. 2(A)). The treatment effect, localized to a predefined retinal region, was shown as a slight decrease in the AF intensity signal due to laser-induced photobleaching. Despite the capability of tracking the anatomical changes, the AF data could not provide any detailed and specific pathology-related information of the molecular changes in the tissue caused by the laser treatment. To overcome these limitations and to improve the diagnostics sensitivity, the FLIM technique has been implemented on the same site (Fig. 2(B)). The treatment effect of the MOPA laser was clearly visible through the blue color footprint of weighted mean fluorescence lifetime  $\tau_m$  which completely matched with the predefined targeted region. . In this region,  $\tau_m$  has increased from  $\tau_m = 700 \pm 50$  ps to  $\tau_m = 820 \pm 50$  ps, shown through a clear blue shift in color-coding. The change in  $\tau_m$  has thus revealed local molecular changes in the RPE tissue while keeping the RPE morphology practically unchanged (see the preservation of RPE honeycomb structure), indicating a mild treatment effect not inducing an undesired RPE damage. Molecular changes observed through the change of the typical fluorescence lifetime for the most abundant lipofuscin granules [33] can be a consequence of localized thermal effect induced by nearby highly absorbing melanin, with its ultrafast energy transfer of laser energy into heat and chemical reactions [34]. In this first experiment, the used laser settings of repetition rate  $\nu = 500$  kHz, average power  $P = 100$  mW,

peak irradiance  $j = 2 \times 10^{10}$  W/cm<sup>2</sup>, fluence  $\varepsilon = 1$  J/cm<sup>2</sup> and dose  $E = 100$   $\mu$ J per pixel were thus found suitable for the treatment that can be monitored and controlled in a real-time using FLIM.

As the technique was found very promising for tracking the molecular changes induced by the laser treatment, it becomes sensible to test and quantify the treatment effect of different laser settings provided by the tunable MOPA laser system. By sweeping through the whole parameter space, described in details in Experimental section, the different treatment effect was observed via FLIM changes (Fig. 3(A)). These remarkable differences were identified inside one order of magnitude change of the laser peak irradiance  $j$ , as will be described in more detail later on. The differences were observed through the measurable molecular alterations in the targeted tissue (see the Sites 1 and 2) caused probably by localized photothermal process changing the chemical properties of the most abundant fluorophore lipofuscin, to the measurable RPE damage, or even the complete RPE destruction both caused by known photomechanical process accompanied with explosive formation micro cavitation bubbles [35,36] (see Sites 3 and 4). The treatment effect measured via  $\tau_m$  ranged from 700 to 800 ps. Lifetime values were, according to the priorly fitted  $\tau$  distribution in the treatment region, fixed to  $\tau_1 = 450$  ps and  $\tau_1 = 1750$  ps giving optimal goodness of fit with least-square distribution  $\chi^2$  of 1 in all stages of treatment effect (see Table. S 1 in the [Supplement 1](#)). The treatment effect was first estimated qualitatively by immediate visual assessment with numbers 1 to 5 according to the extent of the effect.

However, the analysis of tracking the change of  $\tau_m$ , the common approach used in FLIM/FLIO diagnostics [20], might not exhibit the highest sensitivity to the measurable molecular and tissue changes. As the individual lifetime components  $\tau_i$  and their amplitudes  $a_i$  represent direct information of the intrinsic RPE tissue fluorophores and their local environment properties, better sensitivity of the observed tissue changes is expected to be revealed through one of these descriptors. As the extent of local differences in  $\tau_m$  enforced the implementation of a more robust two-exponential model with fixed lifetime values, the most sensitive descriptor for the observed treatment effect was clearly the ratio between the fitted amplitudes of the fluorescence lifetime components  $a_2/a_1$ . Visually accessed estimation of the treatment effect (Fig. 3(A)) was thus nicely translated to the distinct distribution profiles of FLIM  $a_2/a_1$  as well as AF  $I$  descriptors (Fig. 3(B)). The molecular changes in RPE identified through the increase of  $\tau_m$  coincide with the redshift as well as broadening in  $a_2/a_1$  distribution. This means that the short lifetime component of lipofuscin  $a_1$  has decreased and is more susceptible to chemical changes via fast local heat generation induced by nearby highly absorbing melanin [34]. A slight decrease in the fluorescence intensity also indicates more photobleaching of the short lifetime component. Typically, chemical changes and photobleaching are a consequence of photochemical non-thermal damage as a result of generated free radicals by a long low-power laser exposure [36]. In our study, however, it was not the case. By a short ps high-power laser exposure, heating rates were higher than chemical relaxation times, thus reactions in the tissue taking place far from equilibrium. The observed tissue effects can thus be a consequence of these various non-linear mechanisms which can include apart from novel physical interactions also novel chemical reaction pathways and products [37].

The next observed effect was the local photomechanical damage of RPE identified through the morphology change accompanied with even mode widened distribution of  $a_2/a_1$ . In case of RPE destruction, the distribution changes completely, which is due to the detection of other endogenous fluorescence molecules from the targeted region, such as are collagen and elastin originating from choroid and sclera beneath the RPE [38]. This can also be confirmed through the significant increase in the lifetime of the second component, from  $\tau_2 = 1750$  ps to  $\tau_2 = 2250$  ps, indicating different fluorescence origins. Additionally, clear differences were observed in the distribution of the normalized autofluorescence intensity (Fig. 3(B), right column), where its decrease and distribution width follows the extent of the treatment effect. Both descriptors have



been thus found promising for quantification and control the treatment effect, important for e.g. retinal theranostics.

### 3.2. Model function for the automated theranostics procedures

The idea described in Experimental was to formulate a function to linearize the extent of treatment effect going well along with the initial qualitative estimation presented in Fig. 3(A). A model function was formed on 74 experiments showing the broad range of treatment effects that is needed to properly set its boundaries. The set of previously identified descriptors  $a_2/a_1$  from FLIM analysis and  $I$  from AF analysis were enough for an optimal and robust quantification of the laser-induced treatment effect giving:

$$F(p, I) = \begin{cases} A(p_j - p_i) + A(\Delta p_j - \Delta p_i) & \text{if } \frac{\Delta I_j}{I_j} - \frac{\Delta I_i}{I_i} < B \\ A(p_j - p_i) + A(\Delta p_j - \Delta p_i) + \left(1 - e^{-\left(\frac{\Delta I_j}{I_j} - \frac{\Delta I_i}{I_i}\right)^2 / B}\right) & \text{if } \frac{\Delta I_j}{I_j} - \frac{\Delta I_i}{I_i} > B \end{cases}$$

where  $p_{i,j}$  and  $\Delta p_{i,j}$  represent mean and standard deviation of the normal distribution of the ratio  $a_2/a_1$  within the targeted region before (i) and after the treatment (j), whereas  $I_{i,j}$  and  $\Delta I_{i,j}$  mean and standard deviation of the fluorescence intensity distribution within the targeted region before (i) and after the treatment (j) (descriptors schematically presented within marked histograms on Fig. 3(B)). A and B present constants, where A is bound to fluorescence lifetime and B to fluorescence intensity descriptors. A was set in such a way that the extent of the treatment effect introducing the molecular changes in the RPE is quantified with values from 0 to 1, whereas B in such a way that further damage of the RPE is quantified with values from 1 to 3. When the change of the normalized standard deviation of fluorescence intensity before and after the treatment exceeds the particular value defined with constant B, the second term including the Gaussian function is added into the model. When the value of the descriptors in the Gaussian exponent becomes considerably higher than B, the whole term quickly approaches 1. This notation best corresponds to the observed treatment effects where already small RPE damage introduces a significant increase in the variation of the fluorescence intensity in the targeted region, the parameter also quantifying the change in the tissue morphology.

How quantitative evaluation of the treatment effect with value  $F$  meets its initial qualitative estimation, nicely depicts Fig. 3(C) showing a nice linear trend. With this approach of the laser treatment evaluation, the effect on the tissue can be precisely controlled in a way that the treatment stops if the function approaches value 1 before severe photomechanical damage can first appear.

### 3.3. Impact of tunable laser parameters on the treatment effect using the model function

The developed model function algorithm was then used to investigate the treatment effect depending on the chosen set of tunable laser parameters of an adaptive MOPA laser system, recently shown capable of both tissue diagnostics and treatment [30] the multiparametric results are presented in Fig. 4, where each data point corresponds to an individual experiment done with the predefined set of laser parameters. The size of each point corresponds to the measurement errors arising from the limited accuracy of the experimental setup and the limited accuracy of the fitted FLIM diagnostics/descriptors. A separate representation of the impact of individual parameters on the treatment effect shows the best correlation with the laser peak irradiance (Fig. 4(A), left graph) and laser mode, changing between conventional fixed repetition rate and an advanced burst mode (Fig. 4(A), left graph). On the other hand, no particular correlation was observed with laser dose and pulse repetition rate (Fig. 4(A), graphs in the middle). Since each point hides more information about a particular set of laser parameters, results have been represented more dimensionally in a way that the points, in most correlative parameter dependence

with the treatment effect, were color-coded with the used laser dose (Fig. 4(B)). Color-coding was done in a logarithmic scale (see the legend on the left).

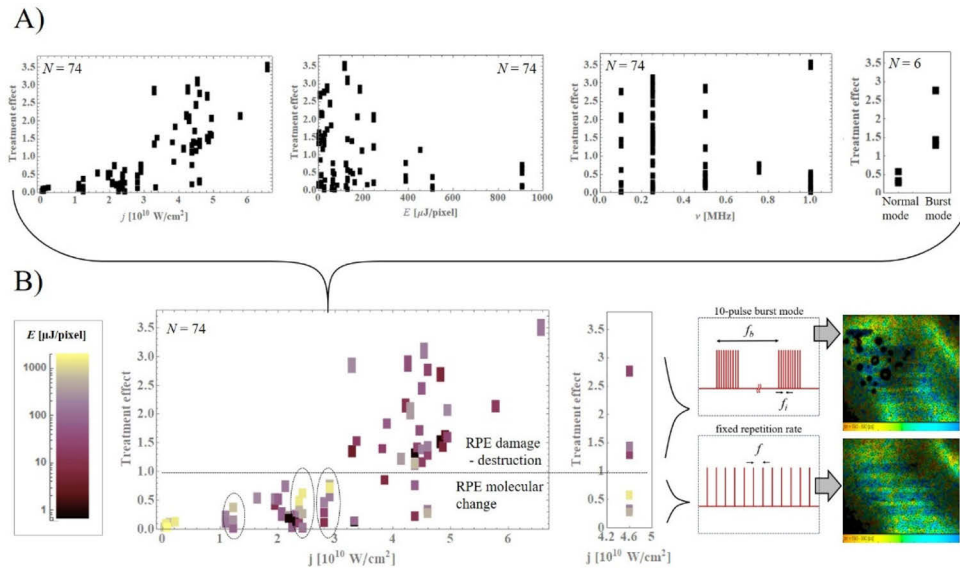


**Fig. 4.** Multi-dimensional representation of the treatment effect defined with model function dependent on the parameters of tunable MOPA laser system. A) Separate representation of the impact of each parameter where the best correlation the treatment effect shows laser peak irradiance (left graph) and laser mode of action (right graph); B) combined representation of the impact of most decisive parameters, laser peak irradiance (x-axis) and laser dose analogous to laser fluence (color coded in logarithm scale). Additional representation of the impact of different pulse mode settings on the treatment effect is shown on the right graphs with the schematics and corresponding FLIM diagnostics.

This multidimensional representation of results focused on the quantification of the treatment effect induced by different laser settings provided a lot of information about the studied system. From the distribution of points, it is evident that laser peak irradiance  $j$  has a crucial role in the treatment effect and that its small increase, from  $j = 3 \cdot 10^{10}$  W/cm<sup>2</sup> to  $j = 4 \cdot 10^{10}$  W/cm<sup>2</sup>, is enough to significantly change the treatment effect, from molecular changes (0 - 1) to the severe RPE damage (1 - 3) (see the two distinct domains split by a horizontal line). This trend was measured irrespective of the laser doses used on the targeted tissue which only confirms the essential role of the laser peak irradiance in such a treatment regime. Furthermore, it is evident that on average, less dose was needed to induce a high treatment effect (1 - 3) compared to the doses needed to induce a low treatment effect (0 - 1) if the threshold intensity was exceeded (see the color-coding in the domains). For example, 100 times higher doses were needed at  $j < 3 \cdot 10^{10}$  W/cm<sup>2</sup> (see the yellow points) to not even closely cause such a treatment effect as measured at  $j > 4 \cdot 10^{10}$  W/cm<sup>2</sup>. This implies on the different laser-tissue interaction mechanisms in the used treatment regime and holds an important message of how laser settings can be wisely adapted in real-time to tune and achieve the desired treatment effect in the targeted tissue. The measurements using intensities below  $j < 3 \cdot 10^{10}$  W/cm<sup>2</sup> also showed a good correlation between the treatment effect (0 - 1) and the laser doses used. This correlation is best observed by comparing the treatment effect and the color-coding of the vertical points at individual laser peak irradiances (see the points inside oval marks). This result shows that the effect in the range 0–1 can easily be adapted by tuning the laser doses once the laser intensity is chosen wisely. Thus, both, peak irradiance and dose were recognized as the process-defining, yet independent parameters.

To fully test the capability of an adaptive MOPA laser system and to better understand pulse mode settings on the treatment effect, the additional measurements were done using two distinct laser modes: 10-pulse burst mode ( $\nu = 0.1$  MHz between bursts and  $\nu = 40$  MHz inside burst) and fixed repetition rate ( $\nu = 1$  MHz) using the same average laser power (Fig. 4(B), right graph and the corresponding schematics of the laser modes). It was immediately evident that burst mode settings induce a significantly higher treatment effect on the tissue ( $> 1$ ) compared to the conventional fixed repetition rate ( $< 1$ ), even at lower doses used. The difference is nicely shown on FLIM diagnostics, where burst mode induces a generation of micro cavitation bubbles, causing severe RPE damage. This difference, as described before, implies the different mechanisms of the laser-tissue interaction in the two regimes, which can be explained in a way that the local heat dissipation rate by an internal conversion and thermal relaxation in the RPE tissue cannot follow the absorbed heat of the laser pulses in individual burst mode that are 25 ns apart ( $\nu = 40$  MHz). Based on the estimated thermal relaxation of the melanin granules as the main absorbers in the RPE being about 300–400 ns [39], the time between the pulses in a burst is at least an order of magnitude faster. Due to relatively high pulse energy delivered in a short laser pulse ( $t = 70$  ps), local heating occurs faster than the heat is capable to diffuse into the surrounding tissue. In other words, the introduction of energy occurs more rapidly than the relaxation time needed to relieve the produced tissue mechanical stress by thermoelastic expansion [36]. The effect on the tissue in the case of the burst mode was thus photomechanical lethal to the surrounding RPE and other cells. Laser pulse shaping in the applied treatment regime using the MOPA laser system can thus be found particularly promising for tuning the local tissue effect, detectable with the model function, through the interplay of different physical laser-tissue interactions. The concept and application of MOPA laser system supported with developed model function for the evaluation of the treatment effect can thus be adopted in any theranostics applications.

The final remaining question is whether the implemented laser parameters can be transferred to an in vivo application? It was recently shown that fixation increases the scattering coefficient of the tissue, but the absorption coefficient remains unchanged [40]. We expect the modification in vivo would require a slight increase in laser power/energy due to the lower scattering coefficient and the fact that light gets partially absorbed in the whole eyes till reaching the retinal tissue. According to this rough approximation, we can expect that in vivo retinal tissue would respond similarly to our ex vivo fixated tissue but using a slightly more powerful range of therapeutic parameters.

#### 4. Conclusion

We have developed a concept and methodology for real-time controlled and quantified tissue theranostics by using a separate synchronized and even single tunable laser system capable of two-photon diagnostics and treatment. Fluorescence lifetime imaging diagnostics approach capable of early detection of RPE degenerative diseases was found particularly sensitive in the evaluation of the extent of the laser-induced tissue effect performed on ex-vivo human RPE as the relevant retinal/eye tissue model. The combination of fluorescence lifetime and autofluorescence intensity parameters, termed descriptors, was then found to best characterize the investigated treatment effect, ranging from local molecular changes in the tissue induced via photothermal effect to the severe tissue modification via photomechanical effect. Based on descriptors, we have proposed and verified an algorithm/function for the quantification of laser-induced tissue changes. It can be particularly useful to control the extent of laser treatment effects through the laser mode adaptation during theranostics operation localized on RPE, aiming to avoid unwanted changes of the surrounding retinal tissue. By additional characterization and evaluation of different impacts of changing laser parameters, from peak irradiance, fluence, pulse repetition rate to mode of operation, on the treatment effect, tunable MOPA laser system could be found particularly promising for theranostics applications in general.

**Funding.** Javna Agencija za Raziskovalno Dejavnost RS (L2-9240, L2-9254, L7-7561, P2-0270).

**Disclosures.** The authors declare no conflicts of interest.

**Data availability.** Data underlying the results presented in this paper are not publicly available at this time but may be obtained from the authors upon reasonable request.

**Supplemental document.** See [Supplement 1](#) for supporting content.

## References

1. T. D. Silva, E. Y. Chew, N. Hotaling, and C. A. Cukras, "Deep-learning based multi-modal retinal image registration for the longitudinal analysis of patients with age-related macular degeneration," *Biomed. Opt. Express* **12**(1), 619–636 (2021).
2. S. S. Kelkar and T. M. Reineke, "Theranostics: combining imaging and therapy," *Bioconjugate Chem.* **22**(10), 1879–1903 (2011).
3. K. König, "Multiphoton microscopy in life sciences," *J. Microsc.* **200**(2), 83–104 (2000).
4. M. S. Cano-Velázquez, N. Davoodzadeh, D. Halaney, C. R. Jonak, D. K. Binder, J. Hernández-Cordero, and G. Aguilar, "Enhanced near infrared optical access to the brain with a transparent cranial implant and scalp optical clearing," *Biomed. Opt. Express* **10**(7), 3369–3379 (2019).
5. K. A. S. M. Saadat, Y. Murakami, X. Tan, Y. Nomura, T. Yasukawa, E. Okada, Y. Ikeda, and Y. Yanagi, "Inhibition of autophagy induces retinal pigment epithelial cell damage by the lipofuscin fluorophore A2E," *FEBS Open Bio* **4**(1), 1007–1014 (2014).
6. A. F. Fercher, K. Mengedoh, and W. Werner, "Eye-length measurement by interferometry with partially coherent light," *Opt. Lett.* **13**(3), 186–188 (1988).
7. W. Drexler, U. Morgner, R. K. Ghanta, F. X. Kärtner, J. S. Schuman, and J. G. Fujimoto, "Ultrahigh-resolution ophthalmic optical coherence tomography," *Nat. Med.* **7**(4), 502–507 (2001).
8. M. van L. Campagne, J. LeCouter, B. L. Yaspan, and W. Ye, "Mechanisms of age-related macular degeneration and therapeutic opportunities," *J. Pathol.* **232**(2), 151–164 (2014).
9. J. Teister, A. Liu, D. Wolters, N. Pfeiffer, and F. H. Grus, "Peripapillary fluorescence lifetime reveals age-dependent changes using fluorescence lifetime imaging ophthalmoscopy in rats," *Exp. Eye Res.* **176**, 110–120 (2018).
10. J. Schmidt, S. Peters, L. Sauer, D. Schweitzer, M. Klemm, R. Augsten, N. Müller, and M. Hammer, "Fundus autofluorescence lifetimes are increased in non-proliferative diabetic retinopathy," *Acta Ophthalmol.* **95**(1), 33–40 (2017).
11. L. Sauer, R. H. Gensure, M. Hammer, and P. S. Bernstein, "Fluorescence lifetime imaging ophthalmoscopy: a novel way to assess macular telangiectasia Type 2," *Oph Retina* **2**(6), 587–598 (2018).
12. D. Schweitzer, L. Deutsch, M. Klemm, S. Jentsch, M. Hammer, S. Peters, J. Haueisen, U. A. Müller, and J. Dawczynski, "Fluorescence lifetime imaging ophthalmoscopy in type 2 diabetic patients who have no signs of diabetic retinopathy," *J. Biomed. Opt.* **20**(6), 061106 (2015).
13. K. Guo, J. Wu, Y. Kong, L. Zhou, W. Li, Y. Fei, J. Ma, and L. Mi, "Label-free and noninvasive method for assessing the metabolic status in type 2 diabetic rats with myocardium diastolic dysfunction," *Biomed. Opt. Express* **12**(1), 480–493 (2021).
14. J. R. Lakowicz, *Principles of Fluorescence Spectroscopy*, 3rd ed (Springer, 2006).
15. K. C. B. Lee, J. Siegel, S. E. D. Webb, S. Lévesque-Fort, M. J. Cole, R. Jones, K. Dowling, M. J. Lever, and P. M. W. French, "Application of the stretched exponential function to fluorescence lifetime imaging," *Biophys. J.* **81**(3), 1265–1274 (2001).
16. A. Periasamy, P. Wodnicki, X. F. Wang, S. Kwon, G. W. Gordon, and B. Herman, "Time-resolved fluorescence lifetime imaging microscopy using a picosecond pulsed tunable dye laser system," *Rev. Sci. Instrum.* **67**(10), 3722–3731 (1996).
17. A. Ehlers, I. Riemann, M. Stark, and K. König, "Multiphoton fluorescence lifetime imaging of human hair," *Microsc. Res. Tech.* **70**(2), 154–161 (2007).
18. B. Leskovic, C. C. Lo, P. R. Hartig, and K. Sauer, "Photon counting system for subnanosecond fluorescence lifetime measurements," *Rev. Sci. Instrum.* **47**(9), 1113–1121 (1976).
19. D. Schweitzer, M. Hammer, F. Schweitzer, R. Anders, T. Doebbecke, S. Schenke, E. R. Gaillard, and E. R. Gaillard, "In vivo measurement of time-resolved autofluorescence at the human fundus," *J. Biomed. Opt.* **9**(6), 1214–1223 (2004).
20. C. Dysli, S. Wolf, M. Y. Berezin, L. Sauer, M. Hammer, and M. S. Zinkernagel, "Fluorescence lifetime imaging ophthalmoscopy," *Prog. Retinal Eye Res.* **60**, 120–143 (2017).
21. J. A. Feeks and J. J. Hunter, "Adaptive optics two-photon excited fluorescence lifetime imaging ophthalmoscopy of exogenous fluorophores in mice," *Biomed. Opt. Express* **8**(5), 2483–2495 (2017).
22. R. Brinkmann, G. Hüttmann, J. Rögener, J. Roider, R. Birngruber, and C. P. Lin, "Origin of retinal pigment epithelium cell damage by pulsed laser irradiance in the nanosecond to microsecond time regimen," *Lasers Surg. Med.* **27**(5), 451–464 (2000).
23. J. Roider, S. H. M. Liew, C. Klatt, H. Elsner, E. Poerksen, J. Hillenkamp, R. Brinkmann, and R. Birngruber, "Selective retina therapy (SRT) for clinically significant diabetic macular edema," *Graefes Arch. Clin. Exp. Ophthalmol.* **248**(9), 1263–1272 (2010).

24. S. Al-Hussainy, P. M. Dodson, and J. M. Gibson, "Pain response and follow-up of patients undergoing panretinal laser photocoagulation with reduced exposure times," *Eye* **22**(1), 96–99 (2008).
25. A. Vogel, M. R. Capon, M. N. Asiyo-Vogel, and R. Birngruber, "Intraocular photodisruption with picosecond and nanosecond laser pulses: tissue effects in cornea, lens, and retina," *Invest. Ophthalmol. Vis. Sci.* **35**(7), 3032–3044 (1994).
26. E. Seifert, J. Tode, A. Pielen, D. Theisen-Kunde, C. Framme, J. Roider, Y. Miura, R. Birngruber, and R. Brinkmann, "Selective retina therapy: toward an optically controlled automatic dosing," *J. Biomed. Opt.* **23**(11), 1–12 (2018).
27. S. Zbinden, S. Kucur, P. Steiner, S. Wolf, and R. Sznitman, "Automatic assessment of time-resolved OCT images for selective retina therapy," *Int. J. CARS* **11**(6), 863–871 (2016).
28. M. Y. Berezin and S. Achilefu, "Fluorescence lifetime measurements and biological imaging," *Chem. Rev.* **110**(5), 2641–2684 (2010).
29. S. Rodimova, D. Kuznetsova, N. Bobrov, V. Elagin, V. Shcheslavskiy, V. Zagaynov, and E. Zagaynova, "Mapping metabolism of liver tissue using two-photon FLIM," *Biomed. Opt. Express* **11**(8), 4458–4470 (2020).
30. R. Podlipiec, J. Mur, J. Petelin, J. Štrancar, and R. Petkovšek, "Two-photon retinal theranostics by adaptive compact laser source," *Appl. Phys. A* **126**(6), 405 (2020).
31. W. Becker, *Advanced Time-Correlated Single Photon Counting Techniques*, Springer Series in Chemical Physics (Springer-Verlag, 2005).
32. J. Petelin, B. Podobnik, and R. Petkovšek, "Burst shaping in a fiber-amplifier chain seeded by a gain-switched laser diode," *Appl. Opt.* **54**(15), 4629–4634 (2015).
33. M. A. Yakovleva, A. S. Radchenko, T. B. Feldman, A. A. Kostyukov, P. M. Arbukhanova, S. A. Borzenok, V. A. Kuzmin, and M. A. Ostrovsky, "Fluorescence characteristics of lipofuscin fluorophores from human retinal pigment epithelium," *Photochem. Photobiol. Sci.* **19**(7), 920–930 (2020).
34. S. Meng and E. Kaxiras, "Mechanisms for ultrafast nonradiative relaxation in electronically excited eumelanin constituents," *Biophys. J.* **95**(9), 4396–4402 (2008).
35. P. Deladurantaye, S. Méthot, O. Mermut, P. Galarneau, and P. J. Rochette, "Potential of sub-microsecond laser pulse shaping for controlling microcavitation in selective retinal therapies," *Biomed. Opt. Express* **11**(1), 109–132 (2020).
36. P. N. Youssef, N. Sheibani, and D. M. Albert, "Retinal light toxicity," *Eye* **25**(1), 1–14 (2011).
37. D. Bäuerle, "Thermal, photophysical, and photochemical processes," in *Laser Processing and Chemistry*, D. Bäuerle, ed. (Springer, 1996), pp. 13–38.
38. E. Borrelli, M. Battista, B. Zuccaro, R. Sacconi, M. Brambati, L. Querques, F. Prascina, S. R. Sadda, F. Bandello, and G. Querques, "Spectrally resolved fundus autofluorescence in healthy eyes: repeatability and topographical analysis of the green-emitting fluorophores," *J. Clin. Med.* **9**(8), 2388 (2020).
39. C. von der Burchard and J. Roider, "RPE and Laser," in *Retinal Pigment Epithelium in Health and Disease*, A. K. Klettner and S. Dithmar, eds. (Springer International Publishing, 2020), pp. 281–292.
40. M. F. G. Wood, N. Vurgun, M. A. Wallenburg, and I. A. Vitkin, "Effects of formalin fixation on tissue optical polarization properties," *Phys. Med. Biol.* **56**(8), N115–N122 (2011).